



Airfoil Aerodynamics in Ground Effect for Wide Range of Angles of Attack

Qiulin Qu,* Wei Wang,[†] and Peiqing Liu[‡]

Beijing University of Aeronautics and Astronautics, 100191 Beijing, People's Republic of China

and

Ramesh K. Agarwal[§]

Washington University in St. Louis, St. Louis, Missouri 63130

DOI: 10.2514/1.J053366

The aerodynamics and flow physics of a NACA 4412 airfoil in ground effect for a wide range of angles of attack from -4 to 20 deg are investigated by numerical simulations. The compressible Reynolds-averaged Navier-Stokes equations and shear-stress transport $k-\omega$ turbulence model equations are solved using the finite-volume method. Analyses of the computed results show that the angle of attack versus height (above the ground) plane can be divided into three regions based on the sign of the lift increment value: region I of positive ground effect, and regions II and III of negative ground effect. For low-to-moderate angles of attack, when the ride height is reduced, the airflow is blocked in the convergent passage between the lower surface of the airfoil and the ground, resulting in increase of pressure on the lower surface of the airfoil. As a consequence, the effective angle of attack decreases, and there is less upward deflection of the streamlines, resulting in an increase in pressure on the upper surface of the airfoil. At high angle of attack, when the ride height is reduced, the adverse pressure gradient along the chordwise direction increases, resulting in a larger region of separated flow. Additionally, for negative angle of attack generating negative lift, the airflow accelerates in the convergent-divergent passage between the lower surface and the ground due to the Venturi effect, resulting in a large suction on the lower surface of the airfoil.

Nomenclature

C_D	= drag coefficient
C_L	= lift coefficient
C_p	= pressure coefficient
c	= chord length of the airfoil
d	= width of local stream tube
d_{in}	= width of the stream tube on the inlet boundary
h	= ride height (i.e., distance between the lowest point of the airfoil surface and the ground)
j	= unit vector along y axis
Ma	= Mach number
n	= unit vector normal to the airfoil surface
p	= local pressure
p_∞	= freestream pressure
Re	= Reynolds number based on chord length
S	= surface area of the airfoil
T	= oscillation period of unsteady aerodynamic forces
V_∞	= freestream velocity
x, y	= Cartesian coordinates with the origin located at the leading edge of the airfoil
y^+	= dimensionless wall distance of the first mesh layer
α	= angle of attack
β	= velocity vector angle (i.e., angle between velocity vector and positive direction of x axis)
Γ	= circulation around the airfoil
ΔC_L	= increment in lift coefficient

Δt = time step for unsteady simulation

$\Delta\alpha$ = increment in angle of attack

ρ = air density

τ = shear stress on the airfoil surface

Subscripts

h = ground effect with the ride height of h

low = lower surface of the airfoil

up = upper surface of the airfoil

∞ = unbounded flow

I. Introduction

WHEN an aircraft flies in proximity to the ground, the airflow around it is forced to become parallel to the ground. The aerodynamics and flow physics in ground effect are different from that in unbounded flow. All airplanes experience ground effect during takeoff and landing, but wing-in-ground (WIG) craft cruising close to water surface actively use ground effect to achieve a high lift-to-drag ratio. Compared to regular airplanes, the aerodynamic efficiency of a WIG craft is higher, which is helpful in improving its fuel efficiency. Compared to regular vessels, the cruising speed of a WIG craft is greater. Therefore, many countries have developed and are developing WIG crafts, and thus there is a great deal of interest in the ground-effect aerodynamics [1–5].

Because a WIG craft usually cruises at low-to-moderate angle of attack (AOA) [2,4], the research in ground-effect aerodynamics has focused primarily on low-to-moderate AOA range, in which the flow remains attached to the surface. Based on the flow physics, ground-effect phenomena can be divided into two categories: the two-dimensional (2-D) chord-dominated ground effect and the three-dimensional (3-D) span-dominated ground effect [5–7]. For a 2-D airfoil at positive AOA, ground proximity generally causes a high-pressure distribution on the lower surface of the airfoil, leading to increase in lift, nose-down pitching moment, and lift-drag ratio; this phenomenon is called the 2-D chord-dominated ground effect. For a 3-D wing at positive AOA, ground proximity often pushes the wing-tip vortices outward along the span, leading to decrease in downwash angle and induced drag; this phenomenon is called the 3-D span-dominated ground effect.

Received 26 January 2014; revision received 20 July 2014; accepted for publication 29 September 2014; published online 5 January 2015. Copyright © 2014 by Qiulin Qu, Wei Wang, Peiqing Liu, and Ramesh K. Agarwal. Published by the American Institute of Aeronautics and Astronautics, Inc., with permission. Copies of this paper may be made for personal or internal use, on condition that the copier pay the \$10.00 per-copy fee to the Copyright Clearance Center, Inc., 222 Rosewood Drive, Danvers, MA 01923; include the code 1533-385X/15 and \$10.00 in correspondence with the CCC.

*Assistant Professor, Institute of Fluid Mechanics; qq@buaa.edu.cn.
Member AIAA.

[†]Graduate student, Institute of Fluid Mechanics; buawangwei@163.com.
Student Member AIAA.

[‡]Professor, Institute of Fluid Mechanics; lpq@buaa.edu.cn.

[§]William Palm Professor, Department of Mechanical Engineering and Materials Science; agarwal@seas.wustl.edu. Fellow AIAA.

For 2-D chord-dominated ground effect, the aerodynamics and flow physics at low-to-moderate AOA have been extensively investigated. Hsien and Chen [8] studied the effect of camber and thickness on the aerodynamics of a 2-D airfoil in ground effect by numerical simulation. They found that the aerodynamic forces on the airfoil were determined by the passage between the lower surface of the airfoil and the ground. Chun and Chang [9] numerically simulated the flowfields around a Clark Y airfoil at $\alpha = 5.92$ deg and a NACA 4412 airfoil at $\alpha = 5$ deg in ground effect using fixed and moving grounds. Their investigation indicated that there were very small differences in lift and pitching moment predictions between the results with fixed and moving grounds; however, the drag in the fixed-ground simulation was smaller than that in the moving-ground simulation. Ahmed et al. [10] reported experimental results for a NACA 4412 airfoil in ground effect at $\alpha = 0 \sim 10$ deg. They found that when the ride height was reduced, the drag increased; however, the lift trend depended on the shape of the passage between the lower surface of the airfoil and the ground, which changed with the AOA. Zerihan and Zhang [11] and Mahon and Zhang [12] performed numerical simulations and wind-tunnel experiments to study the negative ground effect of a Tyrrell-02 airfoil, which is a highly cambered inverted airfoil. For this case, when the ride height decreased, the downward force first increased gradually to a peak value and then decreased dramatically.

For the 3-D span-dominated ground effect, the majority of investigations have focused on the aerodynamics and the trajectories of wing-tip vortices. Moon et al. [13] conducted numerical studies on the influence of aspect ratio on the aerodynamics of a 3-D wing of an aerolevitation electric vehicle (AEV) in ground effect. It was found that the lift-to-drag ratio decreased as the span was reduced, due to the formation of an arch vortex at the junction of main and vertical wings. Chawla et al. [14] studied the effect of end plates on the aerodynamics of a wing with NACA 4415 section and aspect ratio of 2.33 using a fixed ground. The AOA was varied from 0 to 25 deg. They found that the use of end plates significantly improved the lift at small ride height. Cho and Han [15] studied the motion of wing-tip vortices in ground effect using the discrete-vortex method. It was noted that the wing-tip vortices moved outward along the span direction. Additionally, the ground restrained the downward movement of the wing-tip vortices. Lee [16] reported experimental results about the motion of wing-tip vortices of a rectangular wing in ground effect. It was found that the motion of wing-tip vortices could be divided into two stages: 1) downward movement of vortices due to the induced velocity effect, and 2) the slowing down of motion of descending vortices due to the presence of ground and their outward movement along the spanwise direction due to the mirror-image effect from the ground. Harvey and Perry [17] conducted the experiments to study the path of wing-tip vortices in ground effect. They found that the wing-tip vortices first descended to the ground and then rebounded downstream; it was due to the fact that the wing-tip vortices first induced the secondary vortices from the ground, and then these secondary vortices induced the wing-tip vortices to move upward.

In general, a WIG craft is designed to cruise at low-to-moderate AOA; however, it occasionally experiences high-AOA flight (e.g., during the emergency climb to avoid obstacles and due to the effects of high-amplitude water waves and random gusts). It is therefore important in WIG craft design to fully understand its aerodynamic characteristics for a wide range of AOA rather than its performance

only under cruise conditions, which is needed for the flight stability and control. Additionally, all airplanes take off and land at high AOA. Therefore, it is necessary to study the aerodynamics and flow physics of a lifting surface in ground effect for a wide range of AOA for improving both the cruise efficiency and flight safety.

Until now, the archival information about the ground-effect aerodynamics at high AOA has been very limited. Hiemcke [18] has reported experimental results for a NACA 5312 airfoil in ground effect at high AOA. It was found that the attached flow on the airfoil evolved into separated flow when the ride height was reduced at high AOA. However, Hiemcke has not described the physical reasons behind the occurrence of flow separation and the influence of flow separation on the aerodynamic forces. Ying et al. [19] conducted numerical studies on the stall characteristics of a NACA 0012 airfoil in ground effect. They found that the stall AOA decreased with the reduced ride height; however, they did not show the flow structure and explained the reasons behind it.

In this paper, the aerodynamics and flow physics of a NACA 4412 airfoil in ground effect for a wide range of AOA is studied for the first time using the compressible Reynolds-averaged Navier-Stokes equations to account for the effects of turbulence in the computational fluid dynamics (CFD) simulations. First, the numerical method is validated by comparing the CFD results with the available experimental data. Second, the AOA and the ride height metric are divided into three regions based on the computed lift increments. Finally, the aerodynamic characteristics and flow physics for several AOAs covering a wide range are analyzed in great detail.

II. Numerical Method and Validation

A. Physical Model

A NACA 4412 airfoil with $c = 1.0$ m, $Ma = 0.26$, and $Re = 6 \times 10^6$ is investigated. A wide AOA range of $\alpha = -4 \sim 20$ deg (with $\Delta\alpha = 2$ deg) is considered to study both the attached and separated flow patterns in ground effect. For 2-D chord-dominated ground effect, several studies [11,12,18–30] have concluded that the critical ride height (the critical ride height is defined as the minimum height below which the aerodynamics is affected by the ground effect) is approximately $h/c = 1.0$ for low and moderate AOAs. To reduce the number of simulation cases, the relative ride heights of $h/c = \infty, 1.0, 0.8, 0.6, 0.4, 0.2, 0.1$, and 0.05 are considered in this paper. The $h/c = 5.0$ and 2.0 are additionally considered for cases of $\alpha = 4$ and 8 deg.

B. Numerical Method

The rectangular computational domain and the mesh layout for an airfoil in ground effect are shown in Fig. 1. The inlet, outlet, and top boundaries are located $40c$ away from the airfoil, and the bottom boundary is located based on the ride height. The airfoil is set as a no-slip static wall; the inlet, outlet, and top boundaries are pressure-far-field boundaries, and the bottom boundary is a no-slip moving wall with a translational velocity equal to the freestream velocity. A multiblock structured H-type mesh is employed. The mesh is refined in the region between the airfoil and the ground.

The rectangular computational domain and the mesh layout for an airfoil in unbounded flow are shown in Fig. 2. The inlet, outlet, top, and bottom boundaries are all located $40c$ away from the airfoil and are set as pressure-far-field boundary conditions. The airfoil surface

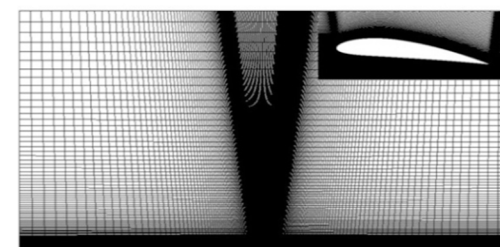
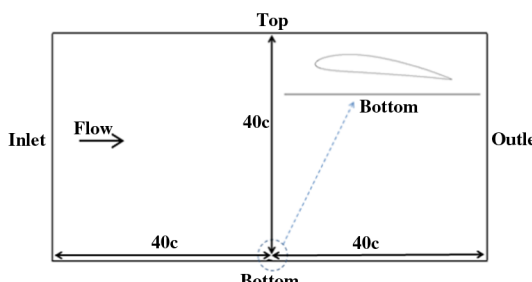


Fig. 1 Computational domain and mesh layout in ground effect.

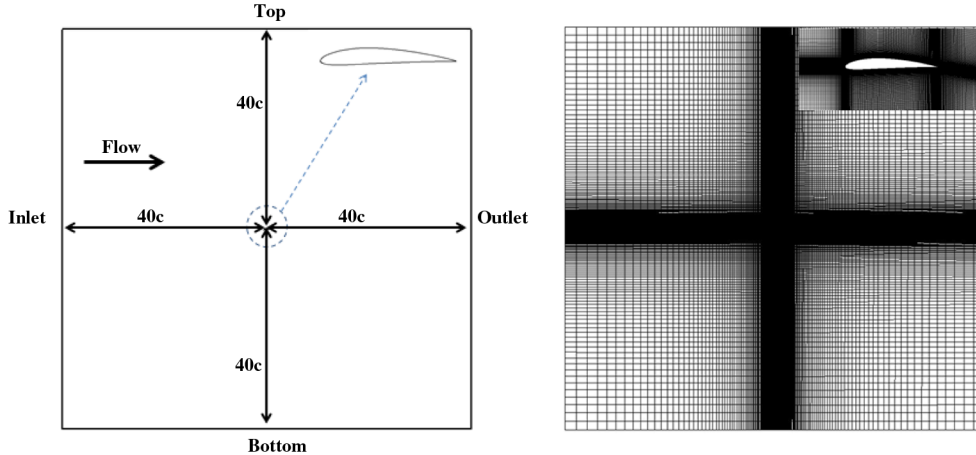


Fig. 2 Computational domain and mesh layout in unbounded flow.

boundary condition and the mesh layout are similar to that in the case of ground effect in Fig. 1.

The double precision solver of ANSYS FLUENT 14.5 is used to perform the CFD simulations. For both steady (in case of attached flow at low-to-moderate AOAs) and unsteady flow (in case of separated flow at high AOA), compressible Reynolds-averaged Navier-Stokes equations with shear-stress transport (SST) $k-\omega$ turbulence model are solved using the finite-volume method. A second-order upwind scheme is used for the convection terms; a second-order central difference scheme is used for the diffusion terms; and a first-order implicit scheme is used for the unsteady terms in the governing equations. The SIMPLE algorithm is used for the pressure-velocity coupling. In the unsteady simulation of separated flow cases, the time step $\Delta t = T/100$ [31] is employed. The converged periodic aerodynamic forces are obtained after 20,000 time steps. The time-averaged aerodynamic forces in one period are used in analyzing the results.

C. Validation of Numerical Method

First, the grid independence of the computed solution is ascertained by computing the flowfield of a NACA 4412 airfoil at $\alpha = 6$ deg, $Ma = 0.26$, and $Re = 6 \times 10^6$ in unbounded flow and in ground effect with $h/c = 0.1$. The results are summarized in Table 1, demonstrating that the medium grid is acceptable for both the lift and drag predictions; therefore, the medium grid is employed in the simulations presented in this paper.

Second, the accuracy of the numerical method for predicting the ground-effect flowfield is assessed by calculating the flowfield of a highly cambered inverted Tyrrell-026 airfoil, widely used in racing cars. The simulation conditions are $\alpha = 3.6$ deg, $h/c = 0.224$, $V_\infty = 30$ m/s, and $Re = 4.6 \times 10^5$, corresponding to the experimental conditions [11]. Our predicted pressure coefficient distribution agrees quite well with the CFD results of Mahon and Zhang [12] and Vogt and Barber [20], as shown in Fig. 3. But compared to the experimental results, the suction peak in all the CFD results is slightly higher. The 2-D and 3-D simulations of the Tyrrell-026 wing have been conducted by Doig and Barber [21]. Their results indicate

that the 3-D effect cannot be ignored completely, although the end plates were installed on the 3-D wing in the experiment [11]; this is the main reason for the difference in the prediction of the suction peak in the 2-D CFD simulation and the 3-D experiment.

Third, the prediction ability of the numerical method for separated flow at high AOA is assessed by calculating the flowfield of a NACA 4412 airfoil at $\alpha = -16 \sim 20$ deg, $Ma = 0.26$, and $Re = 6 \times 10^6$ in unbounded flow. The lift curves from the present CFD result, the NASA experiment [32], and the CFD result from Ockfen and Matveev [24] are compared in Fig. 4. Compared to the experimental data, CFD predictions for the linear part and the nonlinear part (before stall AOA) of the lift curve are very accurate, but the lift coefficients

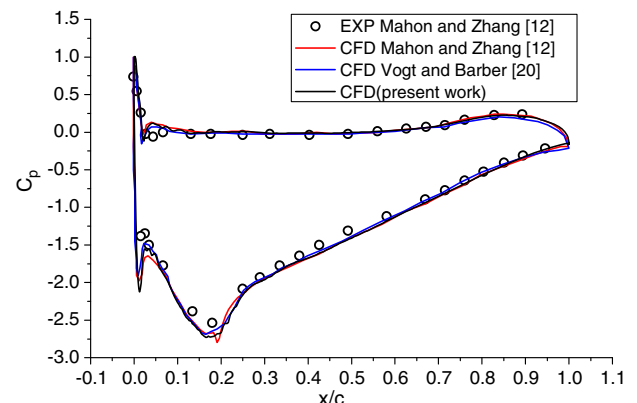


Fig. 3 Pressure coefficient distribution on the Tyrrell-026 airfoil in ground effect.

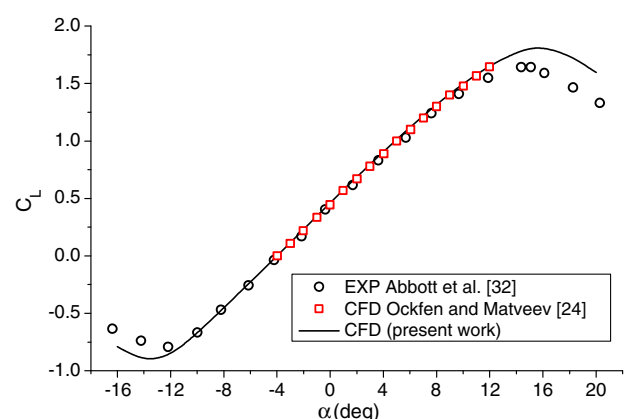


Fig. 4 Lift curves of the NACA 4412 airfoil in unbounded flow.

Table 1 Assessment of grid independence of the computed solution

Mesh	Cell numbers	y^+	C_L	C_D
Unbounded flow				
Coarse	137,000	2	1.1205	0.012025
Medium	250,000	1	1.1194	0.012162
Fine	510,000	2/3	1.1192	0.012180
Ground effect with $h/c = 0.1$				
Coarse	156,000	2	1.2803	0.009365
Medium	316,000	1	1.2746	0.009983
Fine	676,000	2/3	1.2742	0.010089

beyond the stall AOA are overpredicted due to the delayed-prediction of separated flow in CFD calculations. This difference in the CFD predictions and the experimental data in the poststall regime can be attributed to three reasons [33].

1) The SST $k-\omega$ turbulence model employed in the calculations assumes a fully turbulent flow; this assumption generally leads to overprediction of the turbulent eddy viscosities in the boundary layers, resulting in the momentum transfer to the near-wall regions, which allows the boundary layers to push through the adverse pressure gradient regions and thus delay separation [34].

2) The grid densities in the separated flow regions and the boundary layers are not large enough to accurately predict the separated flow.

3) The second-order spatial discretization scheme employed in the present simulation may not be adequate for accurate simulation of separated flow regions on the grids employed.

It should be noted that reasons 2 and 3 are coupled; higher mesh density may be needed with a second-order accurate algorithm, or a higher-order accurate algorithm may be needed on reasonable mesh density to accurately resolve the separated flow region. In general, it

is fair to say that the prediction of separated flow in the poststall region still remains a challenging frontier in CFD.

III. Results and Discussion

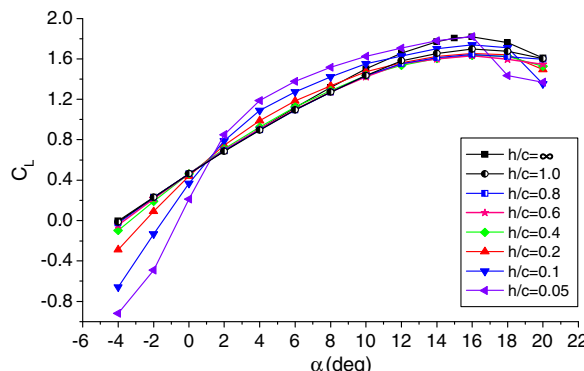
A. Lift Characteristics

For convenience in explaining the results, the following definitions and notations related to lift coefficient are introduced. The total lift coefficient of an airfoil is defined as follows:

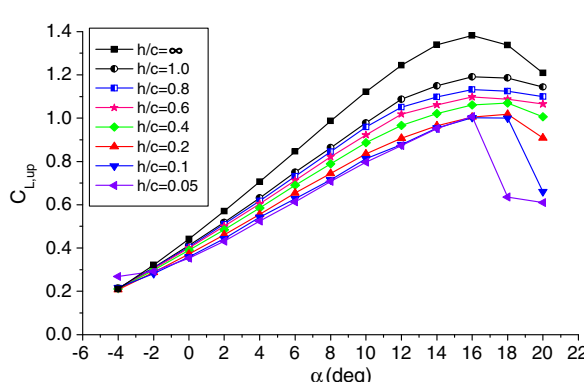
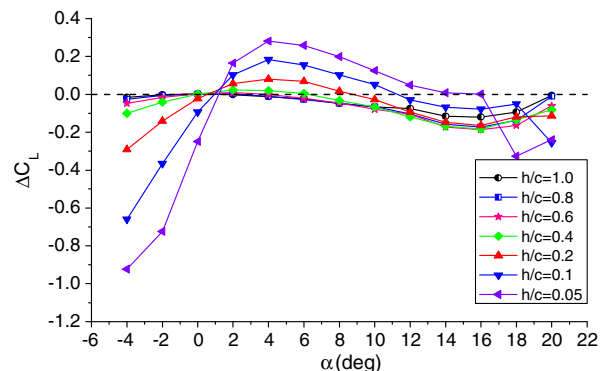
$$C_L = \frac{1}{0.5\rho V_\infty^2 c} \oint_{S_{\text{up}}+S_{\text{low}}} ((p - p_\infty)\mathbf{n} + \boldsymbol{\tau}) \cdot \mathbf{j} dS \quad (1)$$

The upper-surface lift coefficient of an airfoil is defined as follows:

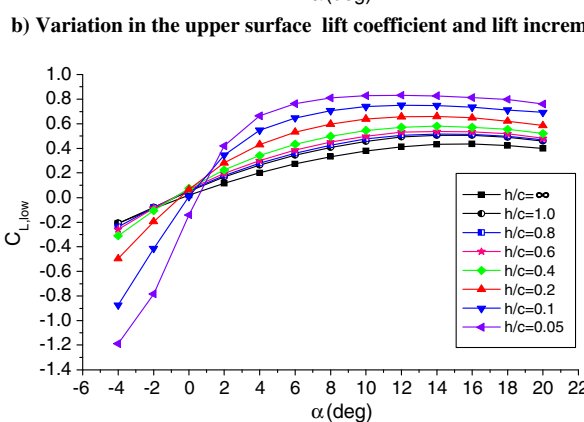
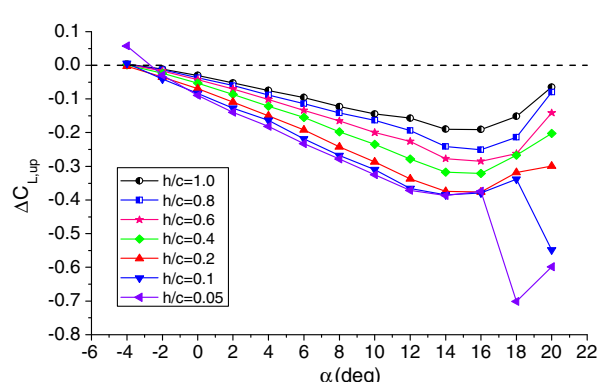
$$C_{L,\text{up}} = \frac{1}{0.5\rho V_\infty^2 c} \oint_{S_{\text{up}}} ((p - p_\infty)\mathbf{n} + \boldsymbol{\tau}) \cdot \mathbf{j} dS \quad (2)$$



a) Variation in the total lift coefficient and lift increment curves with angles of attack at various ride heights



b) Variation in the upper surface lift coefficient and lift increment curves with angles of attack at various ride heights



c) Variation in the lower surface lift coefficient and lift increment curves with angles of attack at various ride heights

Fig. 5 Lift curves and lift increment curves for the NACA 4412 airfoil at various ride heights.

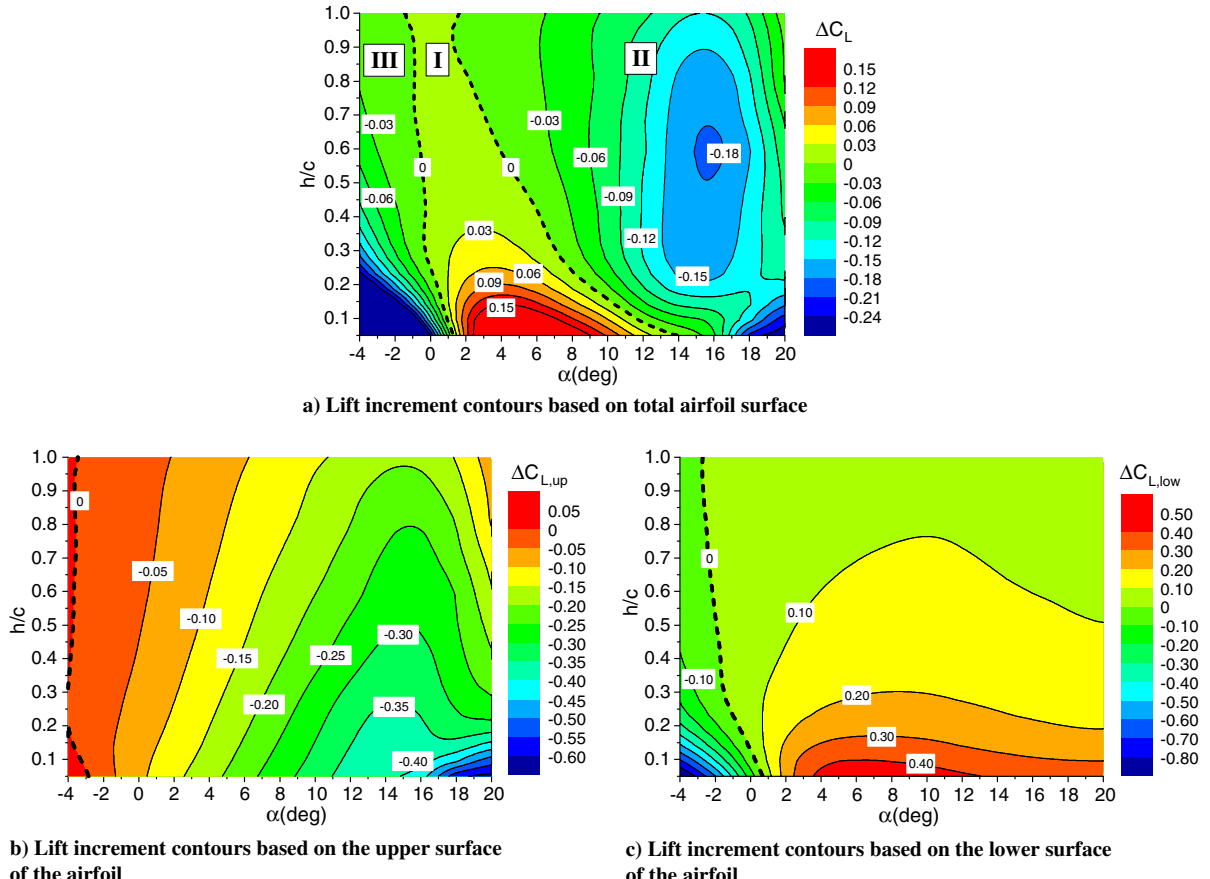


Fig. 6 Lift increment contours of the NACA 4412 airfoil in the AOA vs ride height plane.

The lower-surface lift coefficient of an airfoil is defined as follows:

$$C_{L,\text{low}} = \frac{1}{0.5\rho V_\infty^2 c} \oint_{S_{\text{low}}} ((p - p_\infty) \mathbf{n} + \boldsymbol{\tau}) \cdot \mathbf{j} dS \quad (3)$$

And the total lift is written as

$$C_L = C_{L,\text{up}} + C_{L,\text{low}} \quad (4)$$

For the ground-effect flowfield with ride height h , the lift increment in total, upper-surface, and lower-surface lifts due to ground effect are defined as follows:

$$\Delta C_L = (C_L)_h - (C_L)_\infty \quad (5)$$

$$\Delta C_{L,\text{up}} = (C_{L,\text{up}})_h - (C_{L,\text{up}})_\infty \quad (6)$$

$$\Delta C_{L,\text{low}} = (C_{L,\text{low}})_h - (C_{L,\text{low}})_\infty \quad (7)$$

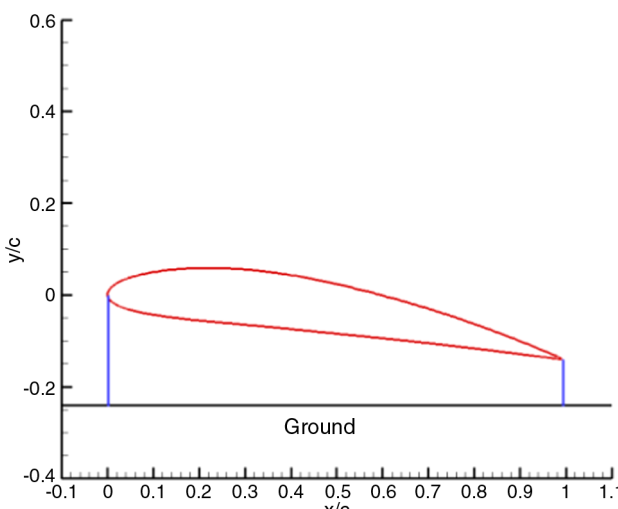


Fig. 7 Convergent passage between the lower surface of the NACA 4412 airfoil and the ground at $\alpha = 8$ deg.

The lift curves and lift increment curves of the NACA 4412 airfoil at various ride heights are shown in Fig. 5. The total lift curve in unbounded flow has an expected linear portion in the AOA range from -4 to 8 deg. However, the total lift curve in ground effect has a convex portion instead of linear portion in this range. Therefore, there are two intersection points between the two lift curves: the lift curve in ground effect and the lift curve in unbounded flow. The smaller the ride height is, the bigger are the curvatures of the convex portion and the AOAs corresponding to the intersection points. In the two regions outside the two intersection points, the lift decreases with the reduced ride height. In the region between the two intersection points, the lift increases with the decreasing ride height; this is the region where the traditional ground-effect aerodynamics research has focused so far. All the cases in unbounded flow and the ground effect for this airfoil have the same stall AOA of 16 deg. However, compared to the unbounded flow, in ground effect the maximum lift is smaller for $h/c = 1.0 \sim 0.1$ and larger for $h/c = 0.05$. The stall characteristics become sharper for $h = 0.1$ and 0.05 .

For all AOAs, the upper surface of the airfoil generates positive lift, which decreases with the reduced ride height. The larger the AOA is, the greater is the decrease in the upper surface lift. For low, moderate, and high AOA, the lower surface produces positive lift, which

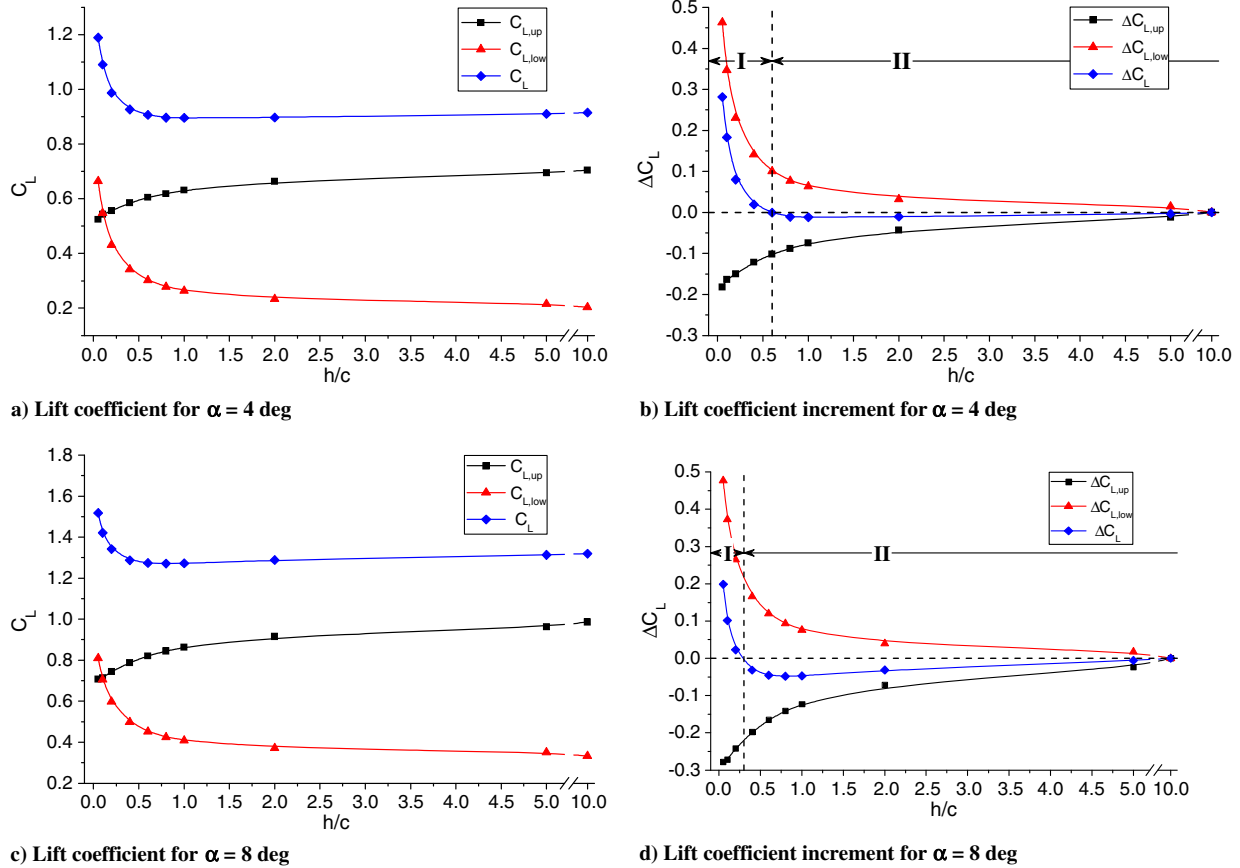


Fig. 8 Variations in lift and lift increment with ride height.

increases with the reduced ride height. For negative AOA, the lower surface produces negative lift, which decreases with the reduced ride height.

Previous investigations [11,12,18–30] determined that the critical ride height is approximately $h/c = 1.0$ for the 2-D chord-dominated ground effect at low and moderate AOAs. From Fig. 5a, one can see that the critical ride height changes with AOA. For negative to moderate AOA (e.g., $-4 < \alpha \leq 8$ deg), the critical ride height can be seen as approximately one chord; but for high AOA (e.g., $8 < \alpha \leq 20$ deg), the critical ride height is larger than one chord. Furthermore, when h/c decreases from ∞ to 1.0, the total lift does not change appreciably for negative to moderate AOA, but the variations in both the upper and lower surface lifts are obvious.

In the AOA versus ride height plane, the lift increment contours of the NACA 4412 airfoil are shown in Fig. 6. Based on the sign of the total lift increment value, the AOA-ride height plane can be divided

into three regions (Fig. 6a): region I of positive ground effect, region II of negative ground effect, and region III of negative ground effect. The lift characteristics and flow physics for the typical AOAs in the three regions are analyzed in detail.

B. Low-to-Moderate Angle of Attack

1. Lift and Pressure Distribution

For the low-to-moderate AOA range, when the ride height decreases, the airfoil enters region I from region II (Fig. 6a). In this AOA range, we analyze the two typical cases with $\alpha = 4$ and 8 deg, where the passage between the lower surface of the airfoil and the ground forms a typical convergent channel, shown in Fig. 7.

Figure 8 presents the variations in lift and lift increment with ride height for $\alpha = 4$ and 8 deg. In the following analysis, the ride height of $h/c = 10$ represents the unbounded flow.

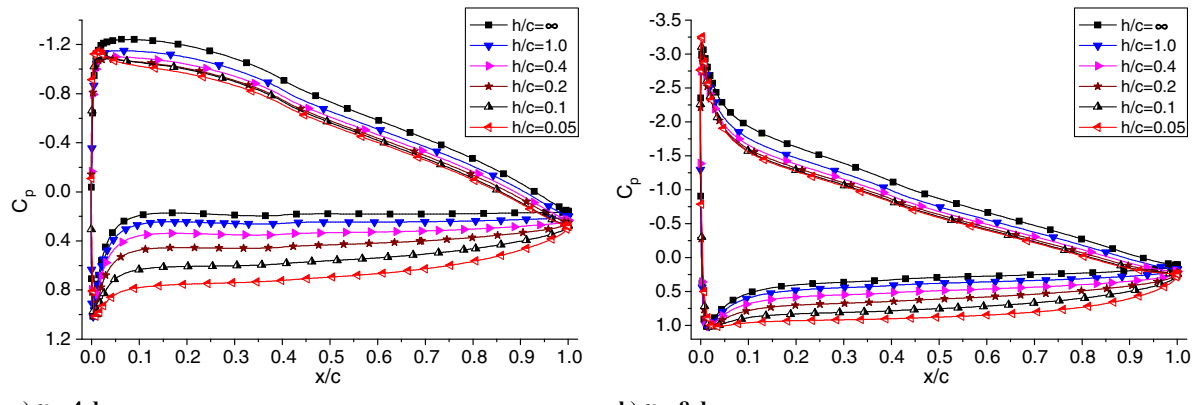


Fig. 9 Pressure coefficient distributions on the NACA 4412 airfoil at various ride heights.

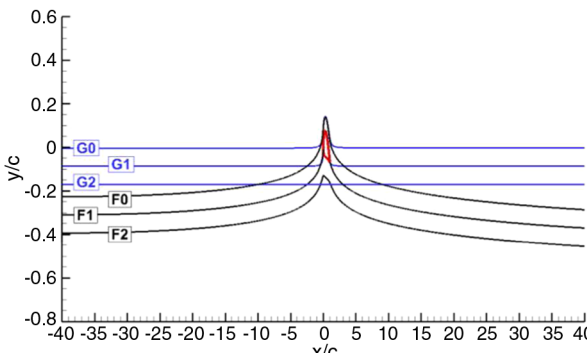
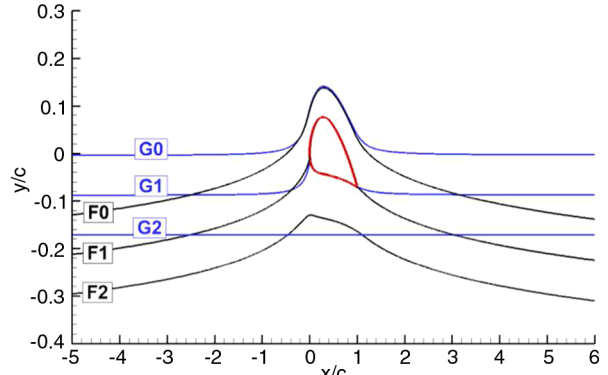
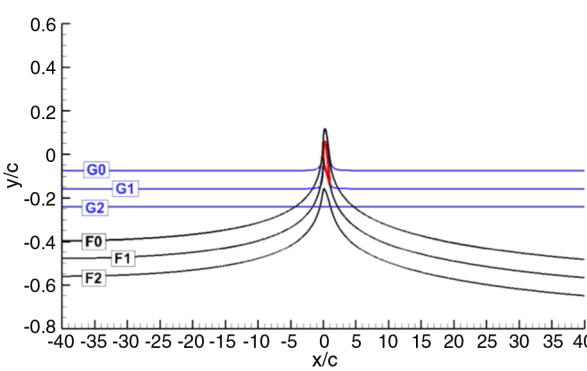
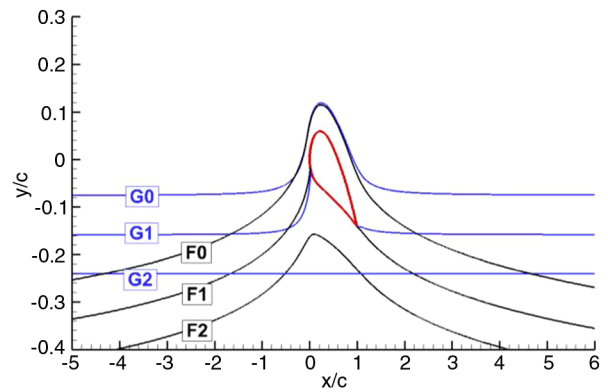
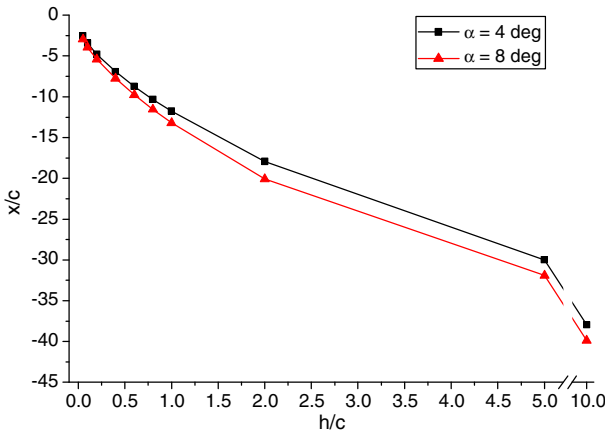
a) Global view of streamlines for $\alpha = 4$ degb) Zoomed-in view of streamlines for $\alpha = 4$ degc) Global view of streamlines for $\alpha = 8$ degFig. 10 Streamlines around the NACA 4412 airfoil: unbounded flow (F0, F1, F2) and ground effect with $h/c = 0.1$ (G0, G1, G2).

Fig. 11 Deflection position of the stagnation streamline with ride height.

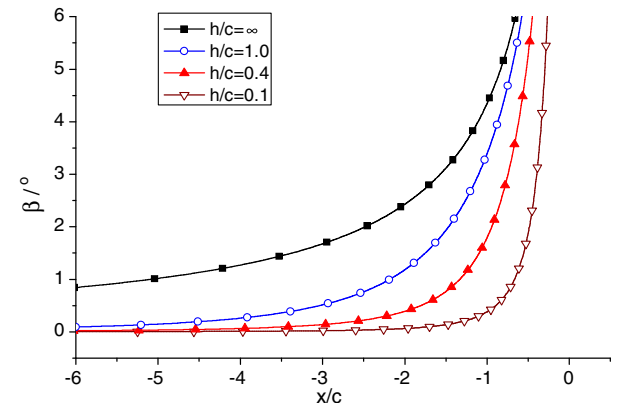
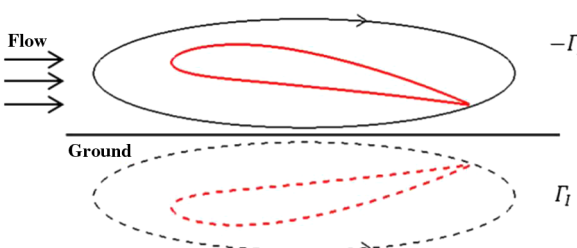
Fig. 13 Velocity vector angle distribution on the stagnation streamline at $\alpha = 8$ deg.

Fig. 12 Mirror-image model of positive ground effect.

In the unbounded flow, $C_{L,up}$ is much greater than $C_{L,low}$. When the ride height decreases, $C_{L,up}$ decreases gradually and $C_{L,low}$ increases gradually. The smaller the ride height is, the faster is the increase in

$C_{L,low}$. Therefore, $C_{L,low}$ becomes larger than $C_{L,up}$ at very small ride height.

At some value of AOA, there is a ride height that results in $\Delta C_L = 0$, which divides the lift increment curve into two regions: lift-reduction region (region II) and lift-enhancement region (region I). The higher the AOA is, the smaller is the ride height that gives $\Delta C_L = 0$; it is $h/c = 0.6$ for $\alpha = 4$ deg and $h/c = 0.3$ for $\alpha = 8$ deg.

From $h/c = \infty$ to the ride height for which $\Delta C_L = 0$, ΔC_L is less than 0 because $|\Delta C_{L,up}| > |\Delta C_{L,low}|$. In this region, the trend of total lift is dominated by the upper surface. From the ride height at which $\Delta C_L = 0$ to $h/c = 0.05$, ΔC_L is greater than 0 because $|\Delta C_{L,up}| < |\Delta C_{L,low}|$, and it increases dramatically. In this region, the trend of total lift is dominated by the lower surface.

Figure 9 shows the pressure coefficient distribution on the NACA 4412 airfoil at various ride heights.

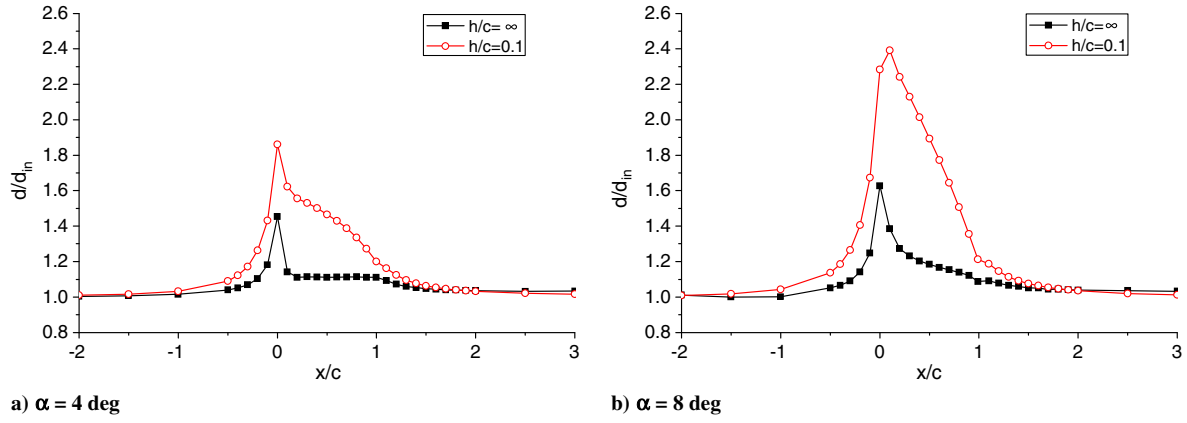


Fig. 14 Width of the stream tube below the NACA 4412 airfoil along the flow direction.

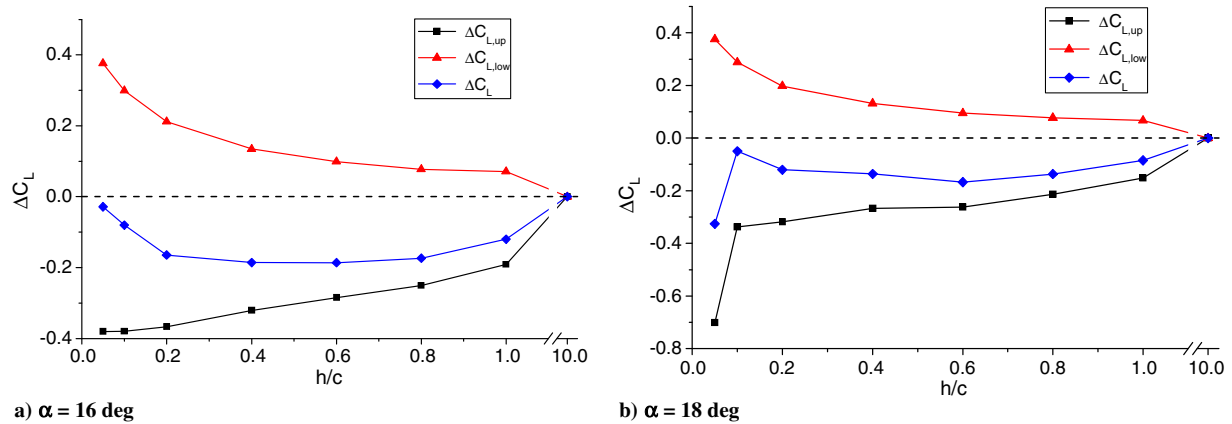


Fig. 15 Variation of lift increment with ride height.

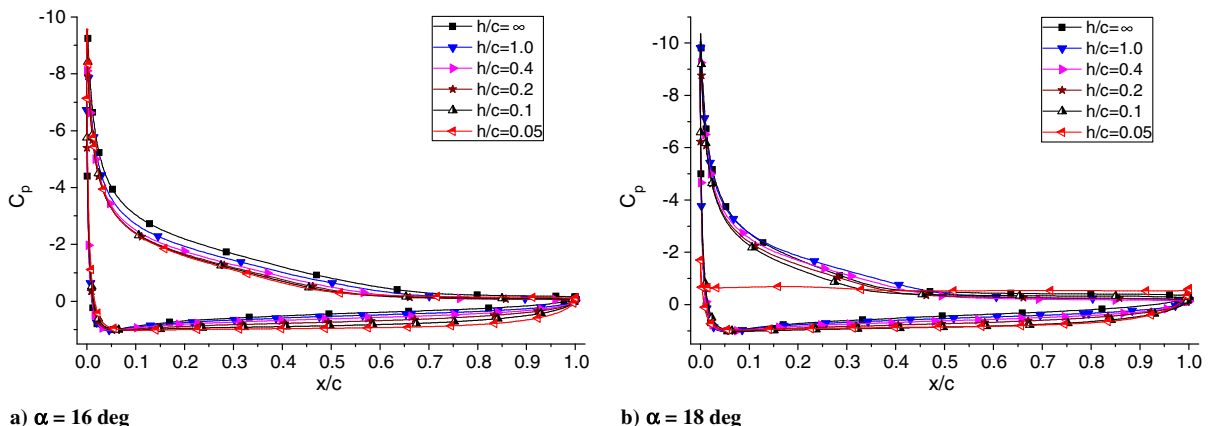


Fig. 16 Pressure coefficient distributions on the NACA 4412 airfoil at various ride heights.

For the two AOAs considered, there is hardly any change in the trend of pressure distribution with ride height. When the ride height is reduced, $C_{p,up}$ increases first quickly and then slowly, resulting in the decrease in $C_{L,up}$; $C_{p,low}$ increases first slowly and then quickly, resulting in the increase in $C_{L,low}$.

From $h/c = \infty$ to $h/c = 0.2$, the suction peak decreases continually to a minimum. When the ride height continues to decrease, the suction peak increases slightly, inducing a larger adverse pressure gradient along the chordwise direction. This is because the stagnation point moves backward, similar to the exposition given by Vogt and Barber [20].

2. Flow Physics

Figure 10 shows the streamlines around the NACA 4412 airfoil in the unbounded flowfield and in the ground-effect flowfield with $h/c = 0.1$.

There are two special streamlines in the flowfield around an airfoil. One terminates at the stagnation point on the airfoil, and the other begins from the trailing edge of the airfoil. The two streamlines are collectively referred to as the stagnation streamline, which divide the upstream inflow into two branches; one goes over the airfoil, and the other goes under the airfoil. In the unbounded flowfield and in the ground-effect flowfield, the stagnation streamline is labeled as F1 and G1, respectively.

The stagnation streamline extends upstream to the inlet boundary at $x/c = -40$ (Figs. 1 and 2). Another two streamlines located above and under the stagnation streamline at an equal distance of $d_{in} = 0.1c$ from it are released from the inlet, which are labeled as (F0, F2) and (G0, G2) for the unbounded flowfield and the ground-effect flowfield, respectively (Fig. 10). Note that the streamline G0 is coincident with the ground for the ground-effect flowfield of $h/c = 0.1$.

For the AOA producing positive lift, the airfoil induces the surrounding streamlines to deflect upward. In the unbounded flowfield, the streamline deflection region is very large from inlet to outlet. However, in the ground-effect flowfield, this region is much smaller and is only in the vicinity of the airfoil. The streamlines G0–G2 remain straight until they approach the leading edge of the airfoil.

Figure 11 shows the deflection of the stagnation streamline with ride height. When the ride height decreases, the position where the deflection begins moves toward the airfoil.

To explain the reduction in streamline deflection in ground-effect flowfield, the mirror-image model [35] for positive ground effect is introduced as shown in Fig. 12. The clockwise circulation around the airfoil is defined as $-\Gamma_1$, and the anticlockwise image circulation below the ground is defined as Γ_1 . In the upstream and downstream regions, the image circulation Γ_1 induces downwash and upwash flow, respectively, which makes the streamlines approach the ground.

In ground effect, the reduction in streamlines' upward deflection produces two results: one of reducing the effective AOA, and the other of blocking the airflow below the airfoil.

Figure 13 shows the velocity vector angle (the velocity vector angle is defined as the angle between the velocity vector and the positive direction of the x axis) distribution on the stagnation streamline at $\alpha = 8$ deg. When the ride height is reduced, the velocity vector angle decreases, resulting in the reduction of effective AOA. The smaller the ride height is, the smaller is the effective AOA.

In both the unbounded flowfield and the ground-effect flowfield, the streamlines (F1 and F2) and (G1 and G2) respectively form a typical stream tube below the NACA 4412 airfoil. Figure 14 shows the width of the stream tube along the flow direction. The tube width almost keeps the same value from the inlet to $x/c = -1$ and then increases sharply to a maximum at $x/c \approx 0$ (corresponding to the leading edge). After that, the width decreases quickly until $x/c = 1$ (corresponding to the trailing edge) and then decreases slowly to the inlet value at $x/c = 2$.

It is clear that the width of the stream tube below the airfoil in the ground-effect flowfield is much larger than that in the unbounded flowfield. This is because the airflow is blocked in the convergent passage below the airfoil; thus, the velocity decreases and the pressure rises. The smaller the ride height is, the more airflow is blocked.

In ground effect, the effective AOA decreases, which would make $C_{p,up}$ increase and $C_{p,low}$ decrease, and the airflow is blocked, which would make $C_{p,low}$ increase. The combination of the two effects makes both $C_{p,up}$ and $C_{p,low}$ increase.

When the ride height decreases from $h/c = \infty$ to the ride height for which $\Delta C_L = 0$, the reduction in effective AOA dominates; thus, $|\Delta C_{L,up}| > |\Delta C_{L,low}|$, and the total lift decreases, resulting in negative ground effect. When the ride height decreases from the ride height for which $\Delta C_L = 0$ to $h/c = 0.05$, the airflow blocking effect dominates; thus, $|\Delta C_{L,up}| < |\Delta C_{L,low}|$, and the total lift increases, resulting in positive ground effect.

C. High Angle of Attack

1. Lift and Pressure Distribution

In the high-AOA range located in region II (Fig. 6a), we analyze the two typical cases with $\alpha = 16$ and 18 deg where the passage between the lower surface of the airfoil and the ground is still a typical convergent channel.

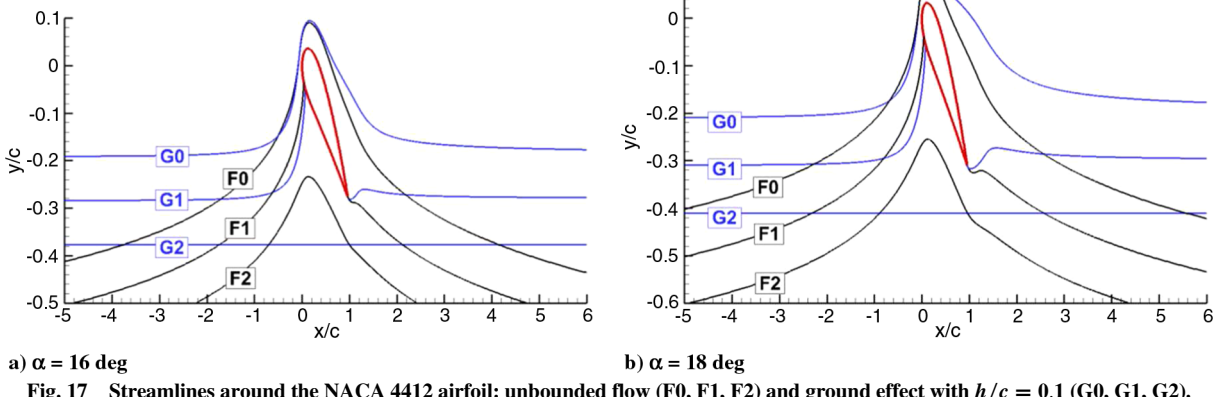


Fig. 17 Streamlines around the NACA 4412 airfoil: unbounded flow (F0, F1, F2) and ground effect with $h/c = 0.1$ (G0, G1, G2).

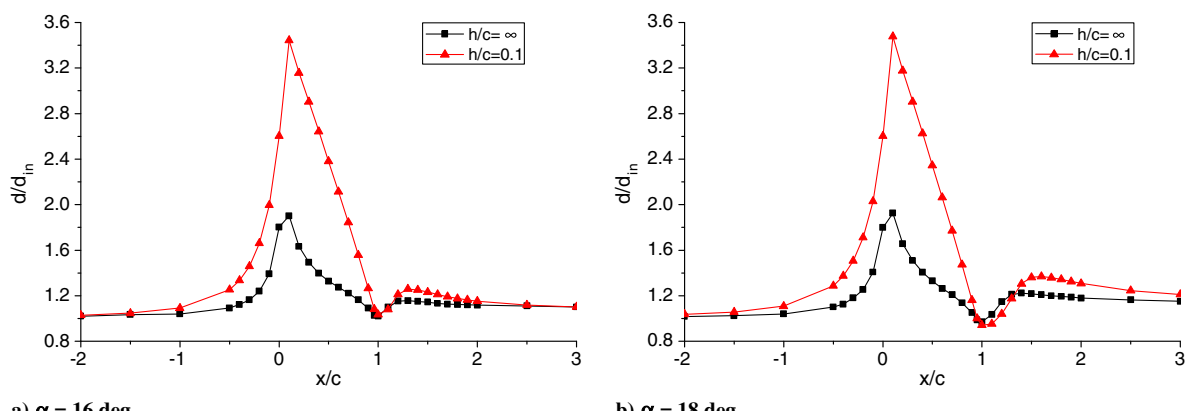


Fig. 18 Width of the stream tube below the NACA 4412 airfoil along the flow direction.

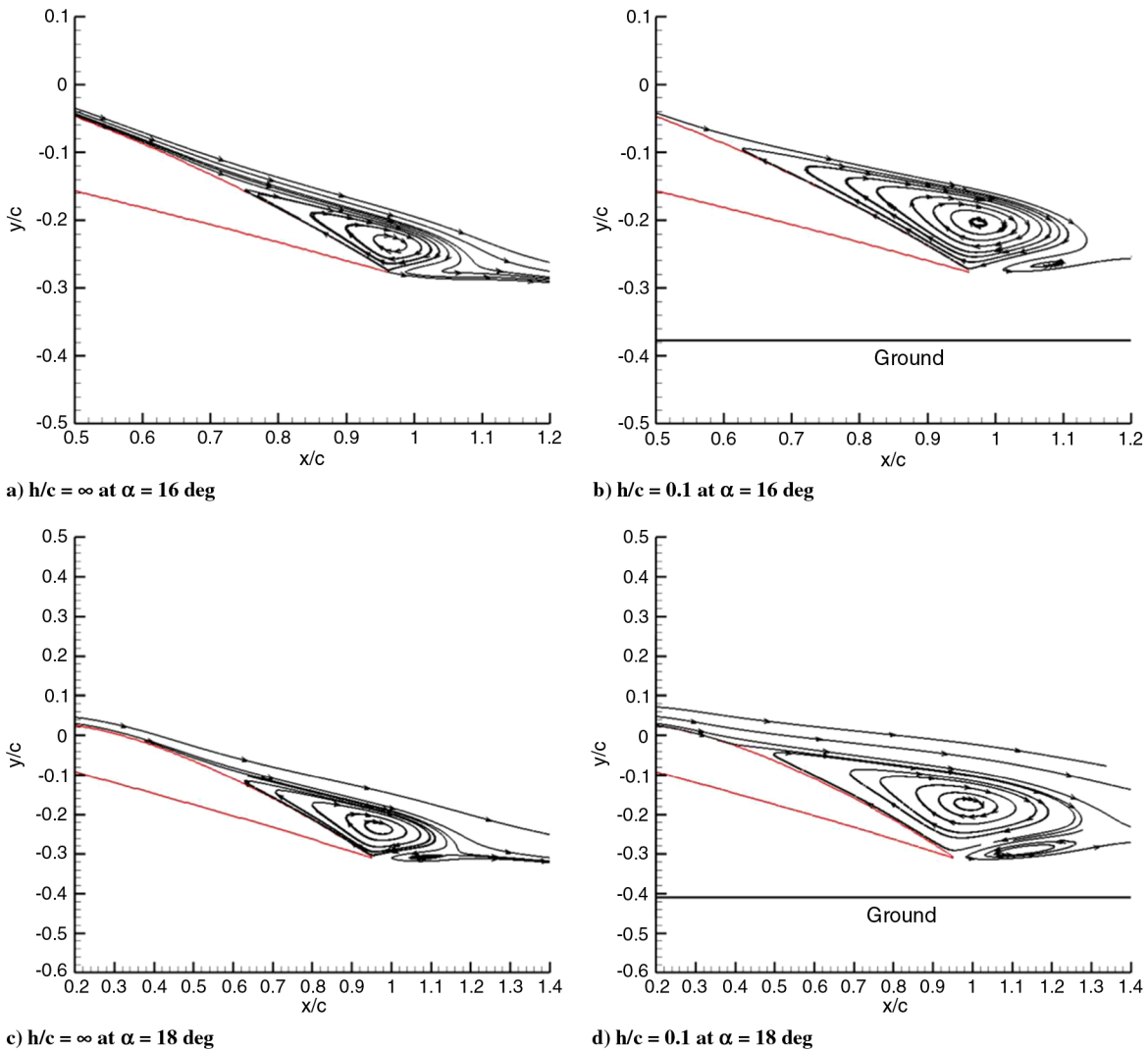


Fig. 19 Steady separated flow region on the upper surface of the NACA 4412 airfoil.

Figure 15 presents the variation of lift increment with ride height. When the ride height is reduced, $\Delta C_{L,up}$ decreases and $\Delta C_{L,low}$ increases. $|\Delta C_{L,up}| > |\Delta C_{L,low}|$ in the entire ride height region, and therefore the total lift increment is negative, resulting in negative ground effect.

Note that $\Delta C_{L,up}$ decreases sharply from $h/c = 0.1$ to 0.05 for $\alpha = 18$ deg; it is because the separated flow suddenly extends to the leading edge of the airfoil.

Figure 16 shows the pressure coefficient distribution on the NACA 4412 airfoil at various ride heights. When the ride height is reduced, $C_{p,up}$ increases quickly and $C_{p,low}$ increases slowly.

In the unbounded flow, when AOA increases, $C_{p,low}$ increases and $C_{p,up}$ decreases. The maximum value of $C_{p,low}$ is limited to 1, but the minimum value of $C_{p,up}$ is unrestricted. Thus, the change in $C_{p,up}$ is larger than that in $C_{p,low}$.

In ground effect, when AOA increases, the pressure increment of the lower surface due to the airflow blocking effect decreases, and the suction decrement of the upper surface due to the reduction of effective AOA increases. Thus, the positive ground effect in region I evolves into the negative ground effect in region II.

There is an obvious pressure plateau region near the trailing edge of the upper surface of the airfoil indicating flow separation. When the ride height is reduced, the pressure plateau region extends toward the leading edge. For the case of $\alpha = 18$ deg and $h/c = 0.05$, nearly the entire upper surface is occupied by the pressure plateau region, which results in a steep reduction in upper surface lift and the total lift due to sharp stall characteristics.

2. Flow Physics

Figure 17 shows the streamlines around the NACA 4412 airfoil in the unbounded flowfield and the ground-effect flowfield at $h/c = 0.1$. Figure 18 shows the width of the stream tube below the airfoil along the flow direction. The main characteristics of streamline deflection and stream tube width are similar to that for the low-to-moderate AOA cases; however, it is a qualitative analysis (based

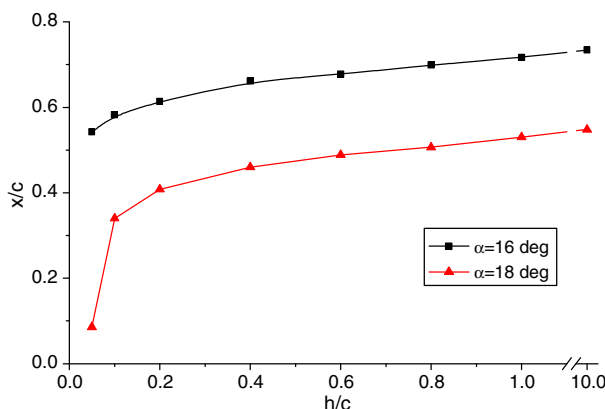


Fig. 20 Position of separation point as a function of ride height.

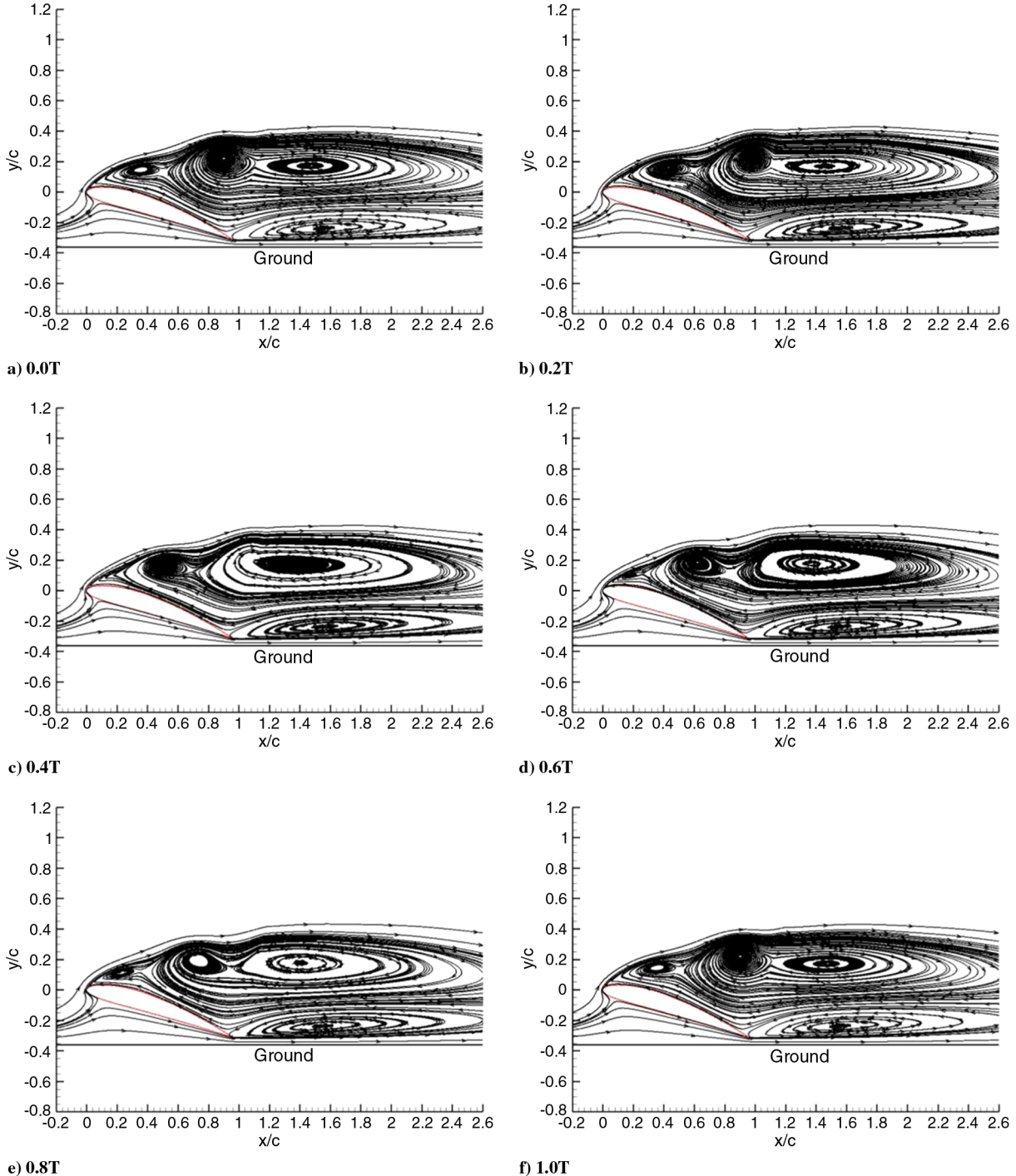


Fig. 21 Unsteady separated flow on the upper surface of the NACA 4412 airfoil at $\alpha = 18$ deg and $h/c = 0.05$.

on less-accurate quantitative information) due to separated flow at high AOA.

For low-to-moderate AOA, the upper surface flow remains attached in both the unbounded flowfield and the ground-effect flowfield; therefore, the streamlines G0 and F0 are almost coincident above the airfoil (see Fig. 10). For high AOA, however, the upper surface separated flow region in the ground-effect flowfield is greater than that in the unbounded flowfield; therefore, the streamline G0 is located above F0 in the vicinity of the airfoil.

Figure 19 shows the steady separated flow pattern on the upper surface of the NACA 4412 airfoil. When the ride height is reduced, the separation point moves toward the leading edge (Fig. 20), and the separation region is enlarged because the adverse pressure gradient along the chord direction increases.

From Fig. 20, it can be noted that the change in the location of the separation point at $\alpha = 18$ deg is very sharp as the ride height changes from $h/c = 0.1$ to 0.05. At $h/c = 0.05$, the separation point is located close to the leading edge, and the separated flow is periodic. Figure 21 shows the unsteady separated flow in one period of oscillation. In the separation region, vortices constantly shed from the leading edge and then merge downstream. The entire upper surface is occupied by the separated flow, resulting in a pressure plateau region on the entire upper surface of the airfoil (Fig. 16b).

D. Negative Angle of Attack

1. Lift and Pressure Distribution

In the negative AOA range located in region III (Fig. 6a), we analyze the typical case of $\alpha = -4$ deg, where the passage between

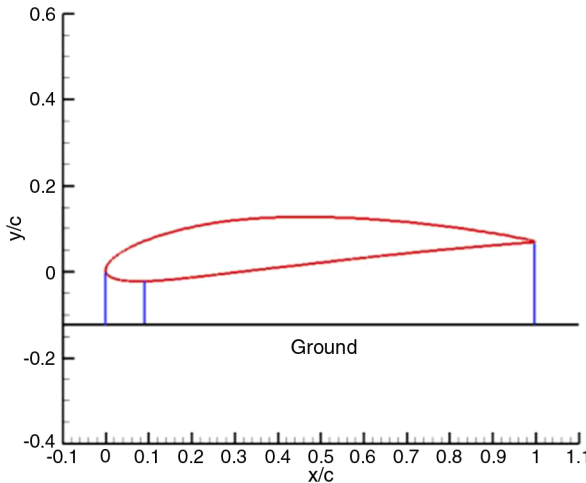


Fig. 22 Convergent-divergent passage between the lower surface of the NACA 4412 airfoil and the ground at $\alpha = -4$ deg.

the lower surface of the airfoil and the ground is a typical convergent-divergent channel like a 2-D Venturi tube (as shown in Fig. 22). Thus, the airflow first accelerates to a maximum velocity at the throat section and then decelerates gradually, resulting in a greater suction peak at the throat section.

Figure 23 presents the variations in lift and lift increment with ride height. When the ride height is reduced, $C_{L,up}$ initially does not change and then increases slightly ($h/c \leq 0.1$), and $C_{L,low}$ decreases first gradually and then dramatically. Thus, the trend in total lift is determined by the lower surface; therefore, C_L decreases with the reduced ride height.

Figure 24 shows the pressure coefficient distribution on the NACA 4412 airfoil at various ride heights for $\alpha = -4$ deg. It is interesting to note that the suction region on the lower surface is apparent due to the Venturi effect. When the ride height is reduced, $C_{p,up}$ initially does not change and then decreases slightly, and thus the suction peak on the lower surface increases and the suction region is enlarged.

2. Flow Physics

Figure 25 shows the streamlines around the NACA 4412 airfoil at $\alpha = -4$ deg. The lift is negative in the entire ride height range (see Fig. 23a); thus, the airfoil induces the surrounding streamlines to deflect downward, which is opposite to what was seen in the previous cases producing positive lift at positive AOA. The reduction in streamlines' downward deflection in ground effect increases the effective AOA.

The mirror-image model of negative ground effect for $\alpha = -4$ deg is shown in Fig. 26. Because the case of $\alpha = -4$ deg in the unbounded flow generates negative lift, the circulation around the airfoil is anticlockwise and is defined as Γ_{III} ; the image circulation below the ground is clockwise and is defined as $-\Gamma_{III}$. In the upstream

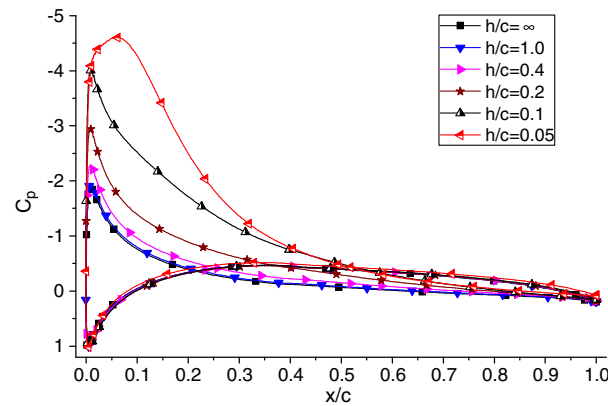


Fig. 24 Pressure coefficient distributions on the NACA 4412 airfoil at various ride heights for $\alpha = -4$ deg.

and downstream regions, the image circulation induces upwash and downwash flow, respectively, which makes the streamlines approach to the ground.

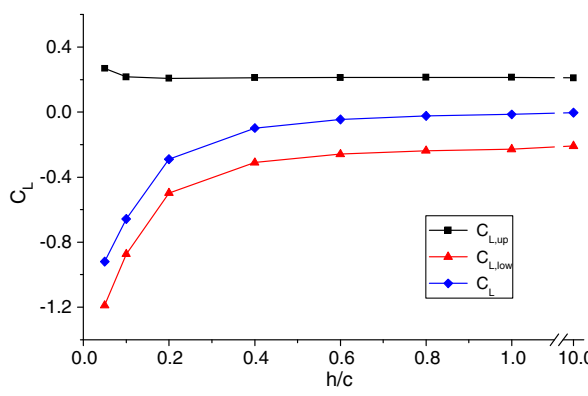
Figure 27 presents the width of the stream tube below the airfoil along the flow direction at $\alpha = -4$ deg. Because the airfoil generates negative lift, the stream tube becomes narrow in the vicinity of the airfoil. The tube width in ground effect is much smaller than that in the unbounded flow due to the Venturi effect; thus, the velocity increases and the pressure decreases. The smaller the ride height is, the more apparent is the Venturi effect.

In ground effect at $\alpha = -4$ deg, the effective AOA increases, which makes $C_{p,up}$ decrease (here, the upper surface is the pressure side) especially at small ride height and $C_{p,low}$ increase (here, the lower surface is the suction side), and the Venturi effect is enhanced, which makes $C_{p,low}$ decrease dramatically. Because the increment effect of effective AOA is much weaker than the Venturi effect, the trend of total lift is decided by the Venturi effect.

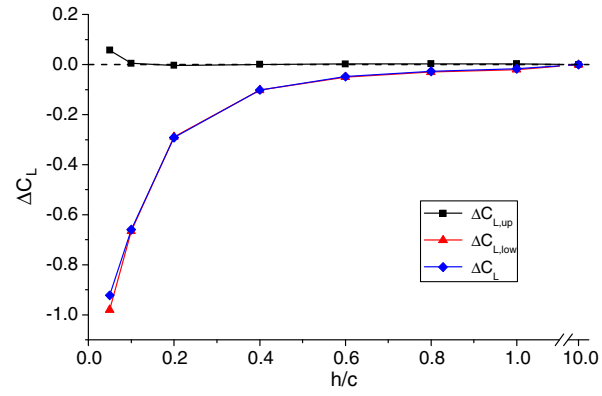
IV. Conclusions

The flowfield of a NACA 4412 airfoil in ground effect is simulated for a wide range of AOA and ride height. The AOA versus ride height plane can be divided into three regions based on the sign of the lift increment value: region I of positive ground effect, and region II and region III of negative ground effect.

1) For low-to-moderate AOA, when the ride height decreases, the airfoil enters region I from region II, and the pressure on the lower surface of the airfoil increases due to the airflow blocking effect from the convergent passage between the lower surface and the ground, and the pressure on the upper surface increases due to the reduction of effective AOA as a result of reduction in streamlines' upward deflection. In region II, the airflow blocking effect is weaker than the reduction effect in effective AOA, resulting in a negative lift increment; in region I, the airflow blocking effect is stronger than the

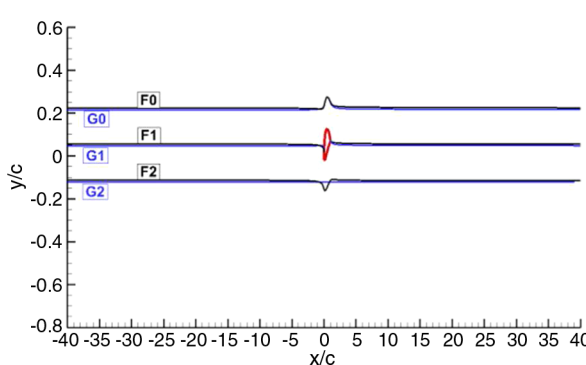


a) Lift coefficient

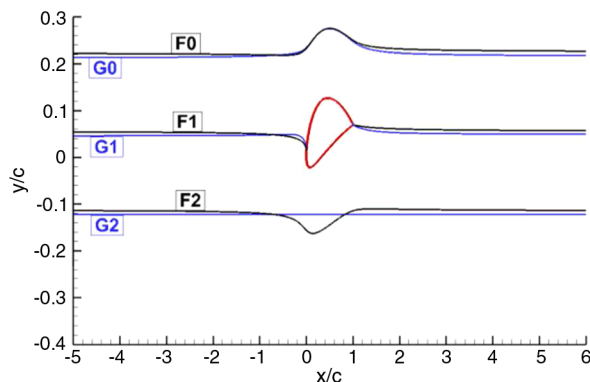


b) Lift coefficient increment

Fig. 23 Variations in lift and lift increment with ride height at $\alpha = -4$ deg.



a) Global view of streamlines

Fig. 25 Streamlines around the NACA 4412 airfoil at $\alpha = -4$ deg: unbounded flow (F0, F1, F2) and ground effect with $h/c = 0.1$ (G0, G1, G2).

b) Zoomed-in view of streamlines

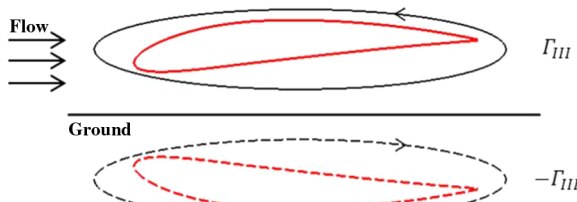
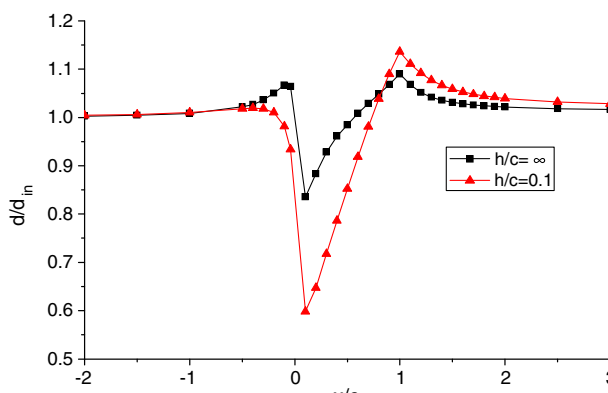


Fig. 26 Mirror-image model of negative ground effect.

Fig. 27 Width of the stream tube below the NACA 4412 airfoil along the flow direction at $\alpha = -4$ deg.

reduction effect in effective AOA, resulting in a positive lift increment.

2) For high AOA located in region II, when the ride height is reduced, the separation point moves toward the leading edge of the airfoil, and the separated flow region is enlarged because the adverse pressure gradient along the chord direction increases. The pressure increment on the upper surface due to the enlarged flow separation region is greater than the pressure increment on the lower surface due to the airflow blocking effect; therefore, the lift increment is negative.

3) For negative AOA located in region III, when the ride height is reduced, the suction on the lower surface increases due to the Venturi effect from the convergent-divergent passage between the lower surface and the ground. The Venturi effect is stronger than the increment effect of effective AOA due to reduced downward deflection of streamlines; therefore, the lift increment is negative.

Acknowledgments

This work was partially supported by the National Natural Science Foundation of China (11302015) and the State Scholarship Fund of China (201203070193).

References

- [1] Qu, Q. L., Lu, Z., Liu, P. Q., and Agarwal, R. K., "Numerical Study of Aerodynamics of a Wing-in-Ground-Effect Craft," *Journal of Aircraft*, Vol. 51, No. 3, 2014, pp. 913–924.
doi:10.2514/1.C032531
- [2] Holloran, M., and O'Meara, S., *Wing in Ground Effect Craft Review*, DSTO Aeronautical and Maritime Research Lab., Melbourne, Australia, Feb. 1999.
- [3] Qu, Q. L., Jia, X., Wang, W., Liu, P. Q., and Agarwal, R. K., "Numerical Simulation of the Flowfield of an Airfoil in Dynamic Ground Effect," *Journal of Aircraft*, Vol. 51, No. 5, 2014, pp. 1659–1662.
doi:10.2514/1.C032452
- [4] Yang, Z. G., and Yang, W., "Complex Flow for Wing-in-Ground Effect Craft with Power Augmented Ram Engine in Cruise," *Chinese Journal of Aeronautics*, Vol. 23, No. 1, 2010, pp. 1–8.
doi:10.1016/S1000-9361(09)60180-1
- [5] Rozhestvensky, K. V., "Wing-in-Ground Effect Vehicles," *Progress in Aerospace Sciences*, Vol. 42, No. 3, 2006, pp. 211–283.
doi:10.1016/j.paerosci.2006.10.001
- [6] Ahmed, M. R., "Aerodynamics of a Cambered Airfoil in Ground Effect," *International Journal of Fluid Mechanics Research*, Vol. 32, No. 2, 2005, pp. 157–183.
doi:10.1615/InterJFluidMechRes.v32.i2.30
- [7] Abramowski, T., "Numerical Investigation of Airfoil in Ground Proximity," *Journal of Theoretical and Applied Mechanics*, Vol. 45, No. 2, 2007, pp. 425–436.
- [8] Hsiun, C. M., and Chen, C. K., "Aerodynamic Characteristics of a Two-Dimensional Airfoil with Ground Effect," *Journal of Aircraft*, Vol. 33, No. 2, 1996, pp. 386–392.
doi:10.2514/3.46949
- [9] Chun, H. H., and Chang, R. H., "Turbulence Flow Simulation for Wings in Ground Effect with Two Ground Conditions: Fixed and Moving Ground," *International Journal of Maritime Engineering*, Vol. 145, No. 3, 2003, pp. 1–18.
doi:10.3940/rina.ijme.2003.a3.29031
- [10] Ahmed, M. R., Takasaki, T., and Kohama, Y., "Aerodynamics of a NACA4412 Airfoil in Ground Effect," *AIAA Journal*, Vol. 45, No. 1, 2007, pp. 37–47.
doi:10.2514/1.23872
- [11] Zerihan, J., and Zhang, X., "Aerodynamics of a Single Element Wing in Ground Effect," *Journal of Aircraft*, Vol. 37, No. 6, 2000, pp. 1058–1064.
doi:10.2514/2.2711
- [12] Mahon, S., and Zhang, X., "Computational Analysis of Pressure and Wake Characteristics of an Aerofoil in Ground Effect," *Journal of Fluids Engineering*, Vol. 127, No. 2, 2005, pp. 290–298.
doi:10.1115/1.1891152
- [13] Moon, Y. J., Oh, H. J., and Seo, J. H., "Aerodynamic Investigation of Three-Dimensional Wings in Ground Effect for Aero-Levitation Electric Vehicle," *Aerospace Science and Technology*, Vol. 9, No. 6, 2005, pp. 485–494.
doi:10.1016/j.ast.2005.01.005
- [14] Chawla, M., Edwards, L., and Franke, M., "Wind-Tunnel Investigation of Wing-in-Ground Effects," *Journal of Aircraft*, Vol. 27, No. 4, 1990, pp. 289–293.
doi:10.2514/3.25270
- [15] Cho, J., and Han, C., "Unsteady Trailing Vortex Evolution Behind a Wing in Ground Effect," *Journal of Aircraft*, Vol. 42, No. 2, 2005,

- pp. 429–434.
doi:10.2514/1.6477
- [16] Lee, T.W., “Experimental Study of Ground Effect on Finite-Wing Wake Flow Development,” M.S. Dissertation, Aeronautics and Astronautics Dept., National Cheng Kung Univ., Tainan City, Taiwan, 2002 (in Chinese).
- [17] Harvey, J., and Perry, F. J., “Flowfield Produced by Trailing Vortices in the Vicinity of the Ground,” *AIAA Journal*, Vol. 9, No. 8, 1971, pp. 1659–1660.
doi:10.2514/3.6415
- [18] Hiemcke, C., “NACA 5312 in Ground Effect: Wind Tunnel and Panel Code Studies,” *15th Applied Aerodynamics Conference*, AIAA Paper 1997-2320, 1997.
doi:10.2514/6.1997-2320
- [19] Ying, C. J., Yang, W., and Yang, Z. G., “Numerical Simulation on Stall of Wing in Ground Effect,” *Flight Dynamics*, Vol. 28, No. 5, 2010, pp. 9–12 (in Chinese).
- [20] Vogt, J. W., and Barber, T. J., “Ground Effect Phenomena About Lift and Downforce Generating Cambered Aerofoils,” *International Journal of Numerical Methods for Heat & Fluid Flow*, Vol. 22, No. 2, 2012, pp. 153–174.
doi:10.1108/09615531211199809
- [21] Doig, G., and Barber, T. J., “Considerations for Numerical Modeling of Inverted Wings in Ground Effect,” *AIAA Journal*, Vol. 49, No. 10, 2011, pp. 2330–2333.
doi:10.2514/1.J051273
- [22] Suh, S., Jung, K., and Chun, H. H., “Numerical and Experimental Studies on Wing in Ground Effect,” *International Journal of Ocean System Engineering*, Vol. 1, No. 2, 2011, pp. 110–119.
doi:10.5574/IJOSE.2011.1.2.110
- [23] Doig, G., Barber, T. J., and Neely, A. J., “The Influence of Compressibility on the Aerodynamics of an Inverted Wing in Ground Effect,” *Journal of Fluids Engineering*, Vol. 133, No. 6, 2011, Paper 061102.
doi:10.1115/1.4004084
- [24] Ockfen, A. E., and Matveev, K. I., “Numerical Study of Wing Aerodynamics in Ground Proximity,” *ASME 2008 International Mechanical Engineering Congress and Exposition*, American Soc. of Mechanical Engineers, New York, 2008, pp. 97–103.
doi:10.1115/IMECE2008-66115
- [25] Djavareshkian, M., Esmaeli, A., and Parsani, A., “Aerodynamics of Smart Flap Under Ground Effect,” *Aerospace Science and Technology*, Vol. 15, No. 8, 2011, pp. 642–652.
doi:10.1016/j.ast.2011.01.005
- [26] Zong, Z., Liang, H., and Zhou, L., “Lifting Line Theory for Wing-in-Ground Effect in Proximity to a Free Surface,” *Journal of Engineering Mathematics*, Vol. 74, No. 1, 2012, pp. 143–158.
doi:10.1007/s10665-011-9497-x
- [27] Jamei, S., Maimun, A., Mansor, S., Azwadi, N., and Priyanto, A., “Numerical Investigation on Aerodynamic Characteristics of a Compound Wing-in-Ground Effect,” *Journal of Aircraft*, Vol. 49, No. 5, 2012, pp. 1297–1305.
doi:10.2514/1.C031627
- [28] Yang, W., Lin, F., and Yang, Z., “Investigation on Application of High-Lift Configuration to Wing-in-Ground Effect,” *Proceedings of the Institution of Mechanical Engineers, Part G: Journal of Aerospace Engineering*, Vol. 226, No. 3, 2012, pp. 260–271.
doi:10.1177/0954410011409488
- [29] Wu, R., Liang, F., and Lin, W. X., “Computational Analysis on Aerodynamics of the Airfoil in Ground Effect,” *Proceedings of the 2012 International Conf. on Computer Science and Electronics Engineering (ICCSEE)*, Vol. 3, IEEE Publ., Piscataway, NJ, 2012, pp. 371–374.
doi:10.1109/ICCSEE.2012.188
- [30] Ahmed, G., “Investigation of Wings in Ground Effect using Computational Fluid Dynamics,” M.S. Dissertation, School of Engineering Sciences, Univ. of Southampton, Southampton, England, U.K., 2012.
- [31] Cummings, R. M., Morton, S. A., and McDaniel, D. R., “Experiences in Accurately Predicting Time-Dependent Flows,” *Progress in Aerospace Sciences*, Vol. 44, No. 4, 2008, pp. 241–257.
doi:10.1016/j.paerosci.2008.01.001
- [32] Abbott, I. H., Von Doenhoff, A. E., and Stivers, L. Jr., “Summary of Airfoil Data,” NASA TM-824, 1945.
- [33] Cummings, R. M., Forsythe, J. R., Morton, S. A., and Squires, K. D., “Computational Challenges in High Angle of Attack Flow Prediction,” *Progress in Aerospace Sciences*, Vol. 39, No. 5, 2003, pp. 369–384.
doi:10.1016/S0376-0421(03)00041-1
- [34] Chitsomboon, T., and Thamtha, C., “Adjustment of $k-\omega$ SST Turbulence Model for an Improved Prediction of Stalls on Wind Turbine Blades,” *Proceedings of the World Renewable Energy Congress*, Vol. 15, May 2011, pp. 4114–4120.
- [35] Mook, D., and Nuhait, A., “Numerical Simulation of Wings in Steady and Unsteady Ground Effects,” *Journal of Aircraft*, Vol. 26, No. 12, 1989, pp. 1081–1089.
doi:10.2514/3.45884

S. Fu
Associate Editor